Biochemistry

 Volume 36, Number 39 September 30, 1997

Accelerated Publications

ESEEM Study of the Phyllosemiquinone Radical $A_1^{\bullet -}$ in ^{14}N- and ^{15}N-Labeled Photosystem I†

Jonathan Hanley, Yiannis Deligiannakis,*,‡ Fraser MacMillan, Hervé Bottin, and A. William Rutherford

Section de Bioénergétique (URA CNRS 2096), Département de Biologie Cellulaire et Moléculaire, CEA Saclay, F-91191 Gif-sur-Yvette, France

Received June 9, 1997; Revised Manuscript Received August 5, 1997⊗

ABSTRACT: The phyllosemiquinone radical of the photosystem I reaction center has been studied by electron spin echo envelope modulation (ESEEM) spectroscopy. A comparative analysis of ESEEM data of the semiquinone in ^{14}N- and ^{15}N-labeled PSI and numerical simulations demonstrate the existence of two protein nitrogen nuclei coupled to the semiquinone. One of the ^{14}N couplings is characterized by a quadrupolar coupling constant $e^2qQ/4h$ of 0.77 MHz, an asymmetry parameter η of 0.18, and a hyperfine coupling tensor with an almost pure isotropic hyperfine coupling, i.e. $(A_{xx}, A_{yy}, A_{zz}) = (1.3, 1.3, 1.5$ MHz). The second nitrogen coupling is characterized by a quadrupolar coupling constant $e^2qQ/4h$ of 0.45 MHz, an asymmetry parameter η of 0.85, and a weak hyperfine coupling tensor with a dominant anisotropic part, i.e. $(A_{xx}, A_{yy}, A_{zz}) = (-0.2, -0.2, 1.5$ MHz). On the basis of a comparison of the ^{14}N-ESEEM data with ^{14}N-NQR and ^{14}N-ESEEM data from the literature, the first coupled nitrogen is assigned to the indole nitrogen of a tryptophan residue. The coupling of the second nitrogen is much weaker and therefore more difficult to assign. However, the simulated spectrum best describes an amino nitrogen of a histidine, although the amide group of an asparagine or glutamine cannot be ruled out. The possible origins of the nitrogen hyperfine coupling are discussed in terms of the amino acid residues thought to be close to the semiquinone in PSI.

Photosystem I is a large multisubunit pigment−protein complex of approximately 300 kDa embedded in the photosynthetic membrane. It is comprised of at least 11 subunits and about 100 chlorophyll molecules (reviewed in ref 1). The general function of PSI[1] is that of a light-driven plastocyanin/ferredoxin oxidoreductase. The redox components involved in the first steps of photoinduced electron transfer are located in the reaction center core complex which is largely hydrophobic and is comprised of subunits PsaA and PsaB. Upon light excitation, the primary electron donor, a dimer of chlorophyll *a* molecules known as P700, forms a highly reducing singlet state which initiates charge separation between P700* and the primary acceptor chlorophyll *a* (A_0). Electrons are then transferred to a phylloquinone, labeled A_1, and then through three iron−sulfur centers before reaching soluble ferredoxin (reviewed in ref 2).

† This work was supported by TMR Grant ERB4001GT957977 (to F.M.), HCM Grant ERBCHRXCT940524, HCM Grant ERB0049GI1901 (to Y.D.), and HFSPO Grant RG0349.

* Corresponding author.

‡Current address: The Institute of Materials Science, NCSR "Demokritos", 15310 Aghia Paraskevi Attikis, Greece.

⊗ Abstract published in *Advance ACS Abstracts*, September 15, 1997.

[1] Abbreviations: PSI, photosystem I; A_0, primary electron acceptor chlorophyll *a*; A_1, PSI phylloquinone secondary electron acceptor; ESEEM, electron spin echo envelope modulation; EPR, electron paramagnetic resonance; NQI, nuclear quadrupole interaction; β-DM, *n*-dodecyl β-D-maltoside; Chl: chlorophyll, F_A, F_B, and F_X, three [4Fe-4S] centers of PSI; HEPES, *N*-(2-hydroxyethyl)piperazine-*N*′-2-ethanesulfonic acid; MES, *2*-(*N*-morpholino)ethanesulfonic acid; PsaA−C, polypeptides coded by the genes *psa*A−C, respectively; Tricine, *N*-[2-hydroxy-1,1-bis(hydroxymethyl)ethyl]glycine; EDTA, ethylenediaminetetraaceticacid

S0006-2960(97)01360-3 CCC: $14.00

The first evidence of two electron transfer components between P700 and the iron−sulfur centers came from the detection of two radicals by EPR spectroscopy following illumination at 200 K under conditions where the iron−sulfur centers were reduced or removed (*3*, *4*). These species were attributed to a chlorophyll anion (A_0^-) and a semiquinone (A_1^-). The latter was unequivocally identified by isotopic labeling (*5*) (for reviews, see refs *2* and *6*).

The three-dimensional structure of PSI has been determined at low resolution (*7*); however, the location of A_1 has not been established. ESEEM spectroscopy has recently been used to characterize hyperfine couplings to semiquinone radicals in the bacterial reaction center and photosystem II (*8*−*11*), providing information on the nature of the amino acid environment of these radicals. In the work described here, we report the comparative analysis of the ESEEM data of the phyllosemiquinone ($A_1^{\bullet -}$) radical in ^{14}N- and ^{15}N-labeled PSI.

MATERIALS AND METHODS

Liquid cultures of wild type *Synechocystis* 6803 were grown in BG11 medium (*12*), buffered with 6 mM HEPES at pH 7.3. Solid cultures were grown on BG11 with 1.5% agar in the absence of HEPES. Uniformly ^{15}N-labeled PSI was isolated from *Synechocystis* cells grown on the same medium as above, containing sodium (^{15}N) nitrate (99% ^{15}N) as the sole nitrogen source. Cells in liquid culture were grown to an OD (820 nm) of ∼1.5, harvested by centrifugation, and broken with a French press, and the cell debris was removed by further centrifugation. Isolated membranes were washed four times with ice cold 20 mM Tricine and 5 mM EDTA at pH 7.8, then resuspended (2 mg/mL chlorophyll) in 20 mM Tricine at pH 8.0, and frozen at 77 K.

Samples (200 μL) in EPR tubes were reduced with sodium dithionite (final concentration of 25 mM and 200 mM glycine at pH 10.0) and then illuminated for 15 s at 200 K (solid CO_2/ethanol) using an 800 W lamp filtered by 4 cm of water and a 720 nm cutoff filter. This treatment was used to fully reduce the iron−sulfur centers. The sample was then further illuminated for 5 min at 220 K followed by 1 min of dark adaptation at 200 K before cooling in the dark to 77 K.

EPR spectra were recorded at liquid He temperatures with a Bruker 300 X-band spectrometer equipped with an Oxford Instruments cryostat. Pulsed EPR was performed with a Bruker ESP 380 spectrometer (*9*). In the three-pulse ($\pi/2-\tau-\pi/2-T-\pi/2$) ESEEM data, the amplitude of the stimulated echo as a function of $\tau + T$ was measured at ∼9.6 GHz and at a magnetic field corresponding to the maximum intensity of the field-swept spectrum of the A_1^-. The minimum interpulse $\tau + T$ was 16 ns and was incremented in steps of 8 ns; the length of the $\pi/2$ pulse was 16 ns. Deadtime reconstruction was performed as in ref *13*. To remove unwanted echoes in the three-pulse experiment, the phase-cycling method in ref *14* was used. Before Fourier transformation, the time domain echo decay was factored out by subtraction of a linear function. Field-swept spectra were obtained by recording the integral of the echo as a function of the magnetic field after a two-pulse sequence ($\pi/2-144$ ns$-\pi$); the $\pi/2$ and π pulses were 16 and 32 ns, respectively, and the integration gate was 200 ns.

The spin Hamiltonian for an $S = {}^1/_2$, $I = 1$ system characterized by an isotropic g tensor with the magnetic field B_0 along z is

$$H = g\mu_B B_0 S_z - g_N \mu_N B_0 I_z + \mathbf{S}\cdot\mathbf{A}\cdot\mathbf{I} + \mathbf{I}\cdot\mathbf{Q}\cdot\mathbf{I} \quad (1)$$

where the hyperfine coupling tensor **A** has principal values (A_{xx}, A_{yy}, A_{zz}) and consists of the isotropic contribution α_{iso} and the traceless tensor **T** describing the anisotropic hyperfine coupling and, for the case of axial symmetry, has principal values ($-T$, $-T$, $2T$). The nuclear quadrupole interaction, **Q**, is traceless by definition. In its principal axis system, the final term in eq 1 is expressed in the form

$$\mathbf{I}\cdot\mathbf{Q}\cdot\mathbf{I} = K[3I_z^2 - I^2 + \eta(I_x^2 - I_y^2)] \quad (2)$$

where K represents the quadrupole coupling constant $e^2qQ/4h$ and η is the asymmetry parameter of the electric field gradient. The energies and eigenfunctions are calculated by numerical diagonalization of the spin Hamiltonian (eq 1), and the three-pulse modulations for each spin-manifold $E_\alpha(\tau,T)$ and $E_\beta(\tau,T)$ and the three-pulse modulations were calculated with the relations derived in ref *15*. In the case of several nuclei coupled to the same electron spin, the resulting modulation functions for each spin manifold were multiplied in the same domain (*15*, *16*) according to

$$E(\tau,T) = {}^1/_2\prod_i E\alpha(\tau,T) + \prod_i E\beta(\tau,T) \quad (3)$$

and the powder average in the time domain is calculated as

$$E_a(\tau,T)_{powder} = \frac{1}{4\pi}\int_{\varphi=0}^{2\pi}\int_{\theta=0}^{\pi} E(\tau,T,\theta,\phi)\sin\theta\, d\theta\, d\phi \quad (4)$$

RESULTS

The X-band EPR spectrum of the phyllosemiquinone (A_1^-) in PSI is shown in Figure 1 (left inset). The signal is at $g = 2.0043 \pm 0.0002$ and has partially resolved hyperfine structure. These characteristics are typical of the semiquinone anion radicals (*17*), (see also ref *5*). At temperatures <15 K, spectra assigned to the reduced iron−sulfur centers were resolved (not shown). These iron−sulfur centers relax much faster than the semiquinone. ESEEM of A_1^- was performed at a high temperature (32 K) to avoid contributions from the iron−sulfur centers in the detected echo, and thus, the modulations originate exclusively from the semiquinone radical.

ESEEM in Unlabeled (^{14}N) PSI. Figure 1A shows the decay of the time domain three-pulse ESE trace. This was recorded at a magnetic field (3457 G) corresponding to the maximum intensity of the echo-detected field-swept spectrum (Figure 1, right inset). The echo decay was recorded at 24 different τ values to avoid missing modulation frequencies due to suppression effects (*18*). The corresponding frequency domain spectra are shown in Figure 1B. In addition to the matrix−proton line at ∼15 MHz, several low-frequency components are resolved at 0.5, 1.7, 2.6, and 2.9 MHz and a broader component with a maximum at ∼4.2−4.5 MHz. The low-frequency components are caused by interactions between the electron spin of A_1^- and nuclear spins which may arise from protons or nitrogen nuclei. To assign the nuclear−electron interaction arising from nitrogen, and thus analyze the nitrogen hyperfine coupling, ESEEM measurements of A_1^- were carried out in both ^{14}N- and ^{15}N-labeled PSI. The nitrogen hyperfine coupling data were then

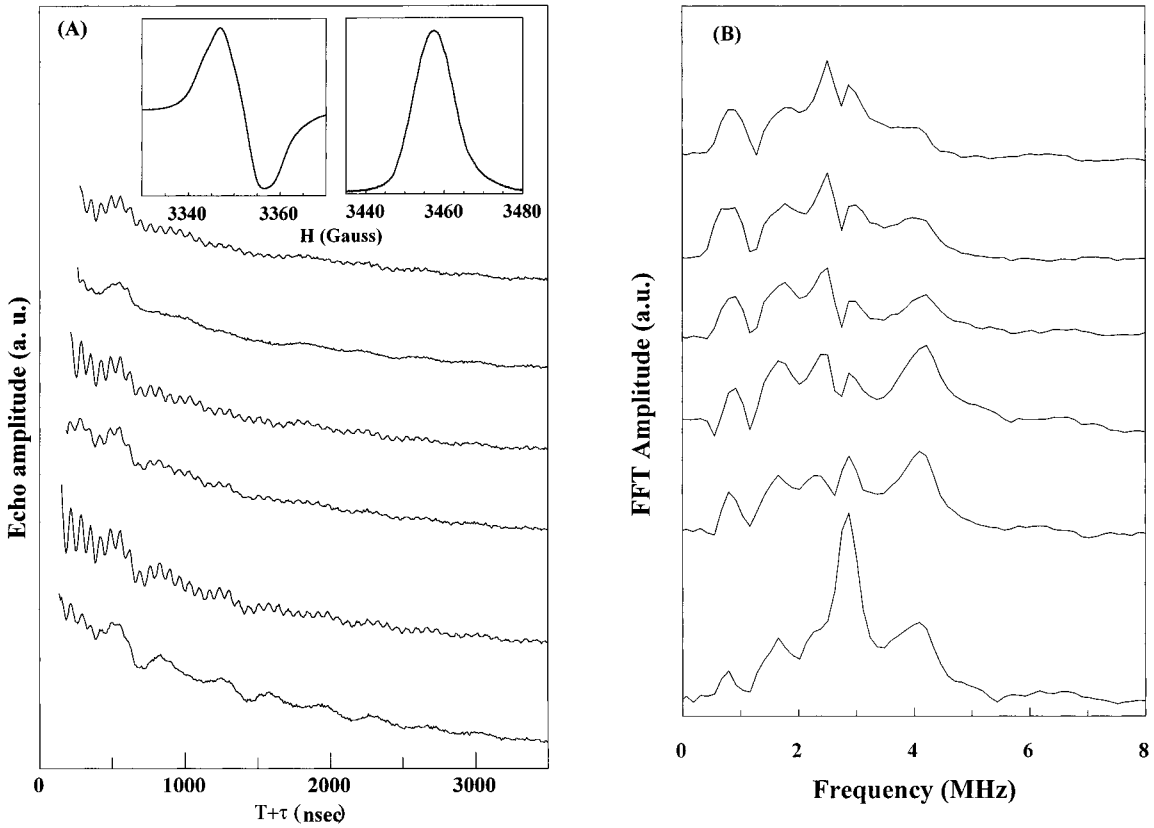

FIGURE 1: Three-pulse ESEEM signal (A) and Fourier transform (B) of $A_1^{\bullet-}$ in [^{14}N]PSI. Experimental conditions were as follows: frequency, 9.65 GHz; magnetic field, 3457 G; temperature, 31 K; time interval between successive pulse sets, 6.4 ms; and 200 events averaged for each time point. For each τ value the initial T value was 40 ns, and 1024 data points were collected at 8 ns intervals; a four-step phase cycle was employed. The τ values from top to the bottom are 380, 312, 260, 244, 168, and 120 ns, respectively; 1024 data points were collected at 16 ns intervals. (Left inset) : X-band continuous wavelength EPR spectrum of $A_1^{\bullet-}$. Experimental conditions were as follows: temperature, 15 K; frequency, 9.42 GHz; power, 50 μW; modulation amplitude, 2 G; and modulation frequency, 100 kHz. (Right inset) Amplitude of the electron spin echo of $A_1^{\bullet-}$ resulting from a two-pulse sequence, as a function of the magnetic field. Experimental conditions were as follows: temperature, 32 K; τ = 144 ns; time interval between successive pulse sets, 6.4 ms; and frequency, 9.65 GHz.

used to determine the nuclear quadrupole coupling parameters for the interacting ^{14}N nuclei.

ESEEM in [^{15}N] PSI. Figure 2A shows representative time domain ESEEM spectra of the semiquinone in [^{15}N]PSI recorded at several τ values. The dominating feature is a modulation of the echo decay with a period of 1.2 μs. Shallower modulations with periods of $\approx$0.7 and $\approx$0.3 μs can be resolved at certain τ values. The frequency domain spectrum is shown in Figure 2B (solid line) and is the sum of 15 τ values (the dashed line is a numerical simulation; see below). In the low-frequency region, there are two strong features at 0.7 and 1.7 MHz. By comparison of the ^{14}N and ^{15}N frequency domain spectra (Figures 1B and 2B, respectively), and from the clear differences in the τ dependence and modulation depths of the spectral features (see Figure 1A and 2A), we conclude that the low-frequency features present in the ^{14}N sample are lost in the ^{15}N sample. This allows an unequivocal assignment of these lines to nitrogen.

Simulations. In an orientationally disordered $S = {}^1/_2$, $I = {}^1/_2$ system, the line shapes for the basic ESEEM frequencies are determined by the angular dependence of the line positions, the modulation depth factor, and the statistical weight factor (*9*, *16*). Generally, the positions of the peaks in the ESEEM spectrum do not correspond to any of the principal values of the hyperfine coupling tensor.

The [^{15}N]semiquinone spectrum shown in Figure 2B has a feature at 1.7 MHz which is close to the Larmor frequency (ν_I) of the ^{15}N nucleus and probably arises from weak hyperfine coupling. The numerical simulations (Figure 2B, dashed line) verify this qualitative view, and the corresponding tensor, labeled tensor I, is characterized by a small α_{iso} = 0.33 MHz which is smaller than the anisotropy part $|T|$ = 0.58 MHz. The simulation indicates that a small part of the peak at 0.7 MHz also originates, partially, from tensor I. The hyperfine coupling for tensor I is listed in Table 1.

Although the peak at 0.7 MHz is partially accounted for by tensor I, the simulated spectra demonstrate that this feature arises predominantly from a second coupled nitrogen nucleus labeled nitrogen II. The type of spectra observed for nitrogen II generally arises from a system where there is only a modest deviation from the "matching condition" i.e.; when $(\alpha_{iso} + T)/4 \sim \nu_I$ (*19*−*21*). In the matching condition, the frequency dispersion arising from the anisotropic hyperfine interactions in the low-frequency nuclear transition vanishes; this is a result of the compensation of dispersive terms bearing opposite algebraic signs. The resulting frequency domain spectrum is characterized by relatively strong narrow features. The numerical simulation shown in Figure 2B demonstrates that tensor II accounts for $\approx$90% of the 0.7 MHz peak and has an α_{iso} of 1.98 MHz and a small anisotropy of $|T|$ = 0.14 MHz. Analogous features have been observed in the ESEEM of [^{15}N]chlorophyll (*22*, *23*) and recently for one of the pyrole nitrogens of the pheophytin

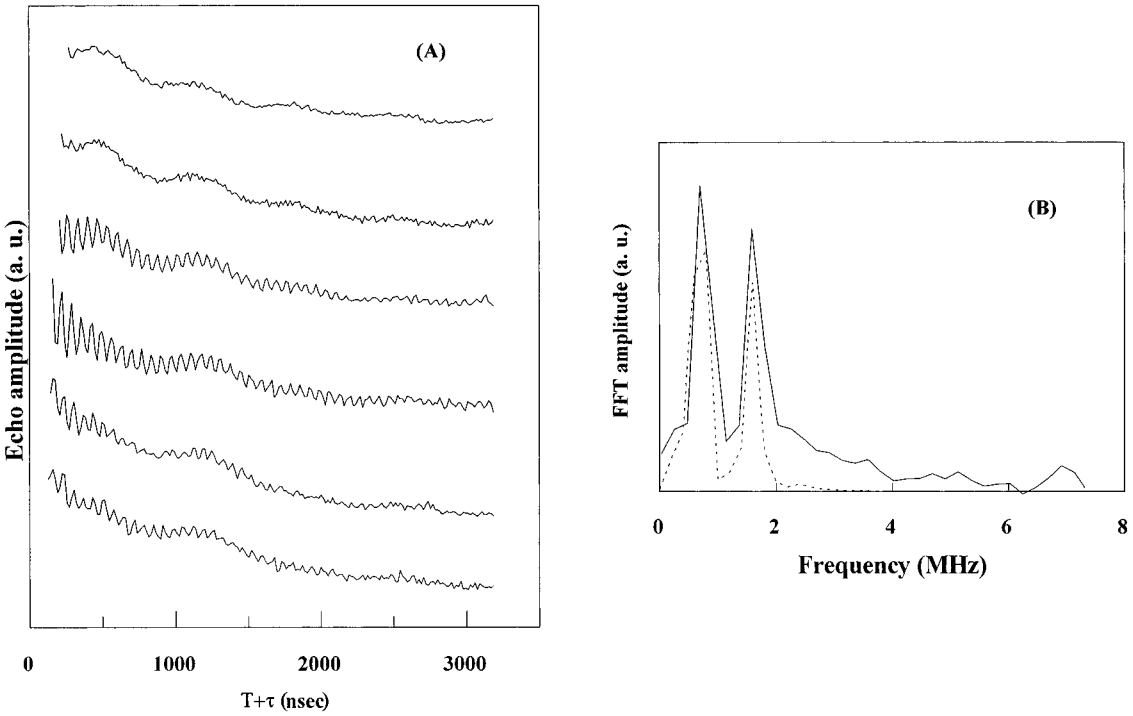

FIGURE 2: (A) Stimulated echo ESEEM signal of $A_1^{\bullet-}$ in [^{15}N]PSI. The τ values are from top to the bottom 376, 328, 280, 256, 160, and 136 ns, respectively. (B) (Solid line) Sum of the Fourier transform of ESEEM recorded at 15 τ values, from 136 to 496 ns in steps of 24 ns. Experimental conditions were as follows: frequency, 9.65 GHz; magnetic field, 3458 G; temperature, 31 K; and other conditions as in figure 1A. (Dashed line) Fourier transform of theoretical simulations of three-pulse ^{15}N-ESEEM spectra obtained with the hyperfine coupling tensors I and II listed in Table 1 and in addition a ^{15}N tensor with principal values (0.15, 0.15, and 0.3 MHz). The spectrum is the sum of 15 spectra calculated for τ values from 136 to 496 ns in steps of 24 ns, including the product rule. Simulation parameters were as follows: frequency, 9.65 MHz; and magnetic field, 3457 G.

Table 1: Stimulated-Echo Modulation Frequencies[a] and Nuclear Quadrupole and Hyperfine Interaction Constants of the $A_1^{\bullet-}$ Radical in ^{14}N- and ^{15}N-Labeled Photosystem I

ESEEM data of $A_1^{\cdot-}$ in PSI										
[^{15}N]PSI				[^{14}N]PSI				published data (^{14}N)		
		hyperfine parameters				NQR parameters		NQR Parameters		
tensor	v (MHz)	α_{iso} (MHz)	T (MHz)	tensor	v (MHz)	K (MHz)	η	K (MHz)	η	ref
I	0.7	0.33	0.58	I	0.5	0.45	0.85	0.80−0.84	0.45−0.51	di/tripeptide[b,c]
	1.7				1.7			0.81−0.83	0.13−0.21	imino His[b,c]
								0.31−0.34	0.91−0.97	amino His[b]
II	1.7	1.98	0.14	II	0.5	0.77	0.18	0.79	0.18	indole Trp[c,d]
					2.6					
								0.98	0.6	amide[c]
					2.9					
					4.2−4.5					

[a] Error ± 0.125 MHz. [b] Ref 28. [c] Ref 27. [d] Ref 26.

anion in [^{15}N]photosystem II (*24*) under conditions of modest deviation from the matching regime. It is worth noting at this point that the τ dependence of the experimental ESEEM spectrum is of primary importance for simulating the spectral features. For example, the frequency position of the feature at 1.7 MHz can also be simulated by a tensor with principal values (0.2, 0.2, 4 MHz); however, the resulting spectrum has a τ dependence that clearly does not fit the experimental trend and can thus be discarded.

In order to account for the relative intensity of the main peaks at 0.7 and 1.7 MHz, we had to add a third ^{15}N tensor which results in additional intensity to the 1.7 MHz peak. This tensor is characterized by a weak hyperfine coupling of $<$0.2 MHz. After being scaled for ^{14}N, this tensor does not result in detectable features.

In summary, the analysis of the ^{15}N data shows that the experimental spectra are described well by two N nuclei coupled to A_1^- and an additional weak "matrix-type" nitrogen coupling. The two main couplings are characterized by hyperfine coupling tensors, I and II, with axial characteristics. These tensors are listed in Table 1. The combination lines arising from multiple nuclear coupling are too weak to be resolved in the present case.

^{14}N Quadrupole Interaction Constants. The analysis of the ^{15}N data allows the determination of hyperfine coupling tensors I and II for two nitrogens interacting with the semiquinone radical in PSI. With the principal values of hyperfine coupling tensors already having been estimated, subsequent analysis of the ^{14}N data allows the estimation of the quadrupole coupling parameters K and η. The prelimi-

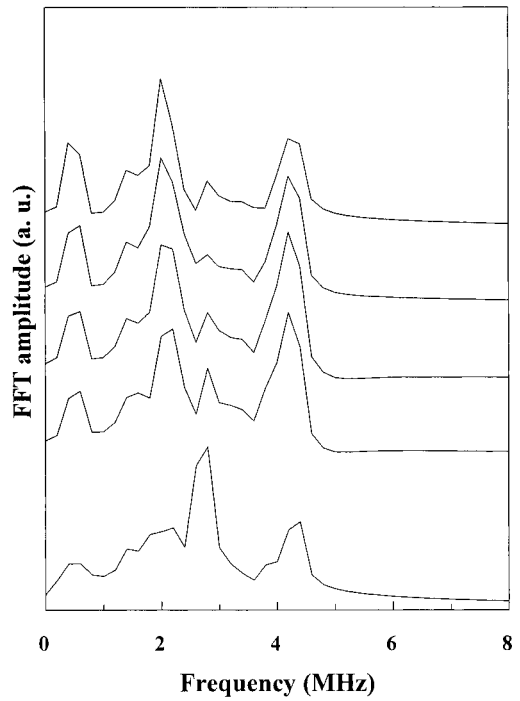

FIGURE 3: Fourier transform of theoretical simulations of three-pulse ^{14}N-ESEEM spectra obtained with the hyperfine coupling tensors I and II listed in Table 1 including the product rule. The τ value is 120 ns for the bottom trace and is increased in steps of 24 ns toward the top. Simulation parameters were as follows: frequency, 9.65 MHz; and magnetic field, 3457 G.

nary fitting of the experimental spectra was directed at the simulation of the frequency positions, i.e. the basic line shapes of the major features in Figure 1B. The Euler angles, defining the relative orientations between the ^{14}N hyperfine and quadrupole coupling tensors, were then adjusted in order to reproduce the correct relative intensities of the individual lines. The simplest situation in ^{14}N-ESEEM spectroscopy is the "exact cancellation condition" $\alpha_{iso}/2 - \nu_I = 0$ (*25*), under which the frequency domain spectra consist of three sharp, low-frequency lines at $\nu_0 = 2K\eta$, $\nu_+ = K(3 + \eta)$, and $\nu_- = K(3 - \eta)$ and a broader feature at higher frequency, typically 4−6 MHz, corresponding to the double-quantum transition. From Table 1, it can be seen that for tensor II, $\Delta = \alpha_{iso}/2 - \nu_I \sim 0.4$ MHz which does not follow the exact cancellation condition. However, Flanagan and Singel (*25*) demonstrated that, if the deviation from the exact cancellation is such that $\Delta < 4K/3\nu_I$, then the simple spectral features characterizing exact cancellation are retained, thus allowing an estimation of the nuclear quadrupole parameters K and η directly from the spectrum. The expected K/ν_I values of the amino acid ^{14}N nuclei in the present study are in the range of 0.5−0.9 MHz which gives $\Delta < 4K/3\nu_I$ (*8*−*11*, *26*−*28*). It is thus expected that the ^{14}N-ESEEM spectrum characterized by tensor II should retain the spectral characteristics of the exact cancellation condition. In agreement with this analysis, the numerical simulations demonstrate that the features at 0.5, 2.6, and 2.9 MHz in Figure 1B correspond to ν_o, ν_-, and ν_+, respectively, while the broader feature at 4.2−4.5 MHz is related to the double-quantum transition.

A series of representative simulated ^{14}N spectra are shown in Figure 3. Euler angles α and γ had no effect on the spectra and were therefore arbitrarily set to zero. The set of nuclear quadrupole parameters for tensor II used to reproduce the experimental spectrum is listed in Table 1.

The spectroscopic features of the coupling defined by tensor I are more difficult to assign qualitatively, and the presence of a dominant anisotropic hyperfine interaction complicates the ESEEM spectra (*29*) (see also ref *24*). The nitrogen coupling defined by tensor II dominates the ^{14}N spectra; therefore, the analysis of tensor I is largely reliant on the numerical simulations. A range of possible K values (0.1 −1.0 MHz) and η values (0−1) were used to simulate the experimental data. There are two sets of K and η values which fit the experimental data; all other combinations introduce simulated spectral features which were clearly absent in the experimental spectrum. For each case, a small deviation of the Euler angles from zero severely diminished the intensity of the observed experimental features; they were thus set at zero. The first set of K, and η values (0.45 MHz and 0.85) gives rise to two spectral features at 1.7 and 0.5 MHz; the second set of values (0.98 MHz and 0.60) gives only one feature at 1.7 MHz. Each of these data sets has the correct experimental τ dependence observed in Figure 1B. The quadrupole parameters used in these simulations are given in Table 1, and the assignment of tensor I is discussed below.

DISCUSSION

The characteristic changes observed in the ESEEM of the phyllosemiquinone radical (A_1^-) in PSI upon isotopic substitution of ^{14}N by ^{15}N demonstrate that the low-frequency modulations arise from nitrogen nuclei coupled to the semiquinone. To identify the origin of these nitrogen nuclei, we rely on comparison of the ^{14}N nuclear quadrupole resonance (NQR) parameters (K and η) derived from the present ESEEM data, with NQR parameters which are available in the literature (*26*−*28*). Such a comparison has been used in analogous ESEEM studies of the semiquinone anion Q_A^- in the photosystem II reaction center (*8*, *9*) and in the bacterial reaction center (*10*, *11*). The NQR data for A_1^- in [^{14}N]PSI from *Synechocystis* 6803 are presented in Table 1. Comparison of the NQR parameters with the published data indicates that the nitrogen coupling which is defined by tensor II (nitrogen II) closely resembles the indole nitrogen of a tryptophan residue.

The coupled nitrogen described by tensor I (nitrogen I) is more difficult to identify; it is characterized by a major feature at 1.7 MHz which fits two sets of NQR parameters. The first set of NQR parameters (K and $\eta = 0.98$ MHz and 0.6, respectively), is representative of an amide nitrogen, and the second set of NQR parameters (K and $\eta = 0.45$ MHz and 0.85, respectively), is representative of an imidazole nitrogen. Fitting the ^{14}N data to the imidazole-like NQR parameters gives rise to two spectral features at 1.7 and 0.5 MHz, and this fits better with the observed experimental data. The simulations thus fit best with the identification of this second residue as a histidine, although the amide side chain of asparagine or glutamine cannot be ruled out.

The isotropic and anisotropic couplings for tensors I and II are listed in Table 1. Tensors I and II are both characterized by small anisotropic hyperfine coupling, whereas the isotropic coupling of tensor II is significantly larger than that of tensor I.

In PSII and bacterial reaction centers, the semiquinone (Q_A^-) shows hyperfine couplings to nearby nitrogen atoms

(*8*−*11*). These couplings are presumed to reflect the presence of hydrogen bonds between imidazole and amide groups on the protein to the carbonyls of the semiquinone. In PSI, ENDOR studies of A_1^- indicate that the semiquinone is hydrogen bonded (*30*; F. MacMillan et al., unpublished); it is reasonable to suggest that tensor I, which is also attributed to an imidazole (or amide) nitrogen, reflects a hydrogen bond from the imidazole (or amide) to the phyllosemiquinone carbonyl. The isotropic and anisotropic couplings for tensor I (Table 1) are consistent with hydrogen bonding, although the couplings are weaker than those seen in PSII and bacterial reaction center semiquinones (*9*−*11*). This may indicate a greater spatial separation or a different geometry between the PSI semiquinone and the interacting nitrogen.

Anisotropic hyperfine coupling results from a dipolar magnetic interaction between electron and nuclear spins. The size of the coupling is determined by the fraction of the electron spin density (ρ_e) which interacts with the nuclear spin and by the interspin distance (*31*). The distance between the coupled nitrogen and A_1^- can be estimated from the point−dipole interaction using the equation $T = \rho_e g_n g_e \beta_n \beta_e / hr^3$, where g_n and g_e are the nuclear and electron g values, respectively, β_n and β_e are the corresponding nuclear and Bohr magneton and r is the distance from the nucleus to the effective position of the electron (*18*). Using this equation, for $\rho_e = 1$, nitrogens I and II are calculated to be 2.4 and 3.7 Å from the spin on the semiquinone, respectively.

The validity of this estimation is compromised by the fact that the electron spin is delocalized over the semiquinone. However, it seems likely that the coupling described by tensor I reflects the presence of a H bond from the protein (an imidazole) to the carbonyl oxygen of semiquinone, and thus, it is probable that the coupling is dominated by the oxygen−nitrogen distance (see ref *9* for a discussion). If so, then the distance estimate can be improved by taking into account the spin density on the oxygen. Spin densities (ranging from 0.19 to 0.23) on the oxygens of semiquinones have been previously measured using ^{17}O-labeled benzoquinones in several environments (*32*, *33*). The value for naphthosemiquinone in a frozen alcoholic solution was measured to be 0.2 (F. MacMillan, unpublished results). Using this estimated spin density, the oxygen−nitrogen distances are thus calculated as ∼1.4 and 2.2 Å. It should be stressed that this distance estimate relies on the assumptions described above and also assumes that semiquinone atoms other than the nearest oxygen have a negligible contribution to the coupling. This distance estimate should thus be taken as a lower limit.

Although tensor II has a weak anisotropic coupling, comparable to that of tensor I, it has a relatively large isotropic interaction. The isotropic hyperfine coupling arises from the non-zero unpaired electron spin density at the nitrogen nucleus (*31*). A possible explanation for the relatively large isotropic coupling observed for tensor II may be the presence of a π-stacking interaction between the tryptophan (identified by the NQR parameters) and the semiquinone. However, the weakness of the anisotropic hyperfine coupling indicates that the indole tryptophan nitrogen (i.e. nitrogen II) is not very close to the semiquinone; the point−dipole calculation for $\rho_e = 1$ estimates the distance to be 3.7 Å. These data are consistent with a π-stacking interaction where the quinone and tryptophan rings are parallel and partially overlapping. The distance of nitrogen II from the quinone ring suggests that the pyrole part of the tryptophan molecule does not overlap the quinone.

The midpoint potential of the PSI phylloquinone is ≈700 mV lower than those of the quinones which act as electron acceptors in PSII and the bacterial reaction center. The low midpoint potential of the PSI semiquinone is presumably brought about by the amino acid environment affecting the electronic structure of the quinone. An interaction comparable to that between the PSI semiquinone and the tryptophan residue reported here does not occur in either PSII or the bacterial reaction center (*8*−*11*). It is therefore possible that this interaction with the tryptophan is at least partially responsible for the low E_m of phylloquinone in PSI.

Structural and functional similarities in type I and type II reaction centers suggested that structural homology existed between the two classes of reaction centers (*7*, *34*−*40*). This idea predicted that the *X*th hydrophobic region of PSI played a role analogous to that of the bacterial reaction center helix D by providing ligands to the reaction center primary donor chlorophylls, P700 (*36*−*38*). Experimental support for the role of helix X in providing a ligand for P700 has been obtained (*41*). Krauss et al. (*7*) have further suggested that a PSI stromal helix, labeled helix n/n′, which links transmembrane helices X and XI, is comparable to the parallel helix (de) linking transmembrane helices D and E in the purple bacteria reaction center. It is thus reasonable to suggest that helix n/n′ may form part of the binding site for A_1 in PSI. The results of the present study indicate that a tryptophan residue forms part of the quinone binding site. From the amino acid sequence for PsaA and PsaB, each of the predicted n/n′ helices has a hydrophobic face that contains a highly conserved tryptophan (PsaA W698 and PsaB W677). Another strongly conserved tryptophan (PsaA W707 and PsaB W686) appears toward the end of this helix which could, from the primary sequence, form part of a hydrophobic loop. It is also interesting to note that the sequence containing these tryptophan residues also contains negatively charged amino acids which could also contribute to the low E_m of the phylloquinone. On the basis of a comparison between the bacterial reaction center and PSI, van der Est et al. (*42*) have also suggested that the sequence of amino acids containing these tryptophan residues may form part of the quinone binding site in PSI. We suggest that one of the residues listed above could be the tryptophan identified in the present study and that it may be homologous to tryptophan 252 from the *Rhodobacter sphaeroides* M subunit. Tryptophan 252 is located between bacteriopheophytin and the quinone in the bacterial reaction center, and it appears to be important for electron transfer between these components (*43*).

The ESEEM data presented here also indicate that there is an interaction of the semiquinone with a second ^{14}N-

[2] While this paper was being prepared, a paper appeared in which it was reported that no nitrogen couplings could be seen from A_1^- in PSI from spinach (*44*). This is in clear disagreement with the present work. We note however that the data shown in ref *44* comparing the relative size of the modulations from A_1^- and A_0^- are similar to those seen in our laboratory (not shown) except that the data in ref *44* have a level of noise which does not allow low-frequency modulations in A_1^- to be reliably distinguished. Therefore, we consider the fact that the apparent discrepancy arises due to the weakness of the A_1^- signal and/or insufficient signal accumulation in ref *44* and that this led to the ^{14}N modulations being overlooked.

containing residue which has NQR parameters consistent with it being a histidine. However, it must be noted that this nitrogen tensor has very weak coupling and the assignment is based largely on one well-resolved peak at 1.7 MHz and a less well resolved peak at 0.5 MHz. There are conserved histidines at positions 689 and 719 in PsaB and at 709 and 735 in PsaA, any of which could hydrogen bond with the phyllosemiquinone. However, structural comparison of the purple bacteria reaction center to PSI tends to favor histidine 719 and 735 (PsaB and PsaA) as a likely hydrogen bonding residue because it lies six residues into the transmembrane helix XI at the stromal side of the membrane.

Although the ESEEM experiments described here indicate the presence of a tryptophan and possibly a histidine residue close to the quinone in PSI, it is not yet possible to identify their exact position in the primary sequence of the protein. However, on the basis of structural, functional, and evolutionary comparisons, the two conserved tryptophan and histidine residues seem to be interesting candidates for site-directed mutagenesis studies[2] .

ACKNOWLEDGMENT

We thank T. A. Mattioli, S. Un, and M. Knüpling for useful discussions and J. McCracken (Michigan State University) for kindly proving a program for the simulation of ESEEM spectra.

REFERENCES

1. Golbeck, J. H. (1994) in *The Molecular Biology of Cyanobacteria* (Bryant, D. A., Ed.) pp 319−360, Kluwer Academic Publishers, Dordrecht, The Netherlands.
2. Brettel, K. (1996) *Biochim. Biophys. Acta 1318*, 322−373.
3. Bonnerjea, J. R., and Evans, M. C. W. (1982) *FEBS Lett. 148*, 313−316.
4. Gast, P., Swarthoff, T., Ebskamp, F. C. R., and Hoff, A. J. (1983) *Biochim. Biophys. Acta 722*, 163−175.
5. Heathcote, P., Moènne-Loccoz, P., Rigby, S. E. J., and Evans, M. C. W. (1996) *Biochemistry 35*, 6644.
6. Snyder, S. W., and Thurnauer, M. C. (1993) *in The Photosynthetic Reaction Center* (Deisenhofer, J., and Norris, J. R., Eds.) Vol. II, Academic Press, San Diego.
7. Krauss, N., Schubert, W. D., Klukas, O., Fromme, P., Witt, H. T., and Saenger, W. (1996) *Nat. Struct. Biol. 3*, 965−973.
8. Astashkin, A. V., Kawamori, A., Kodera, Y., Kuroiwa, S., and Akabori, K. (1995*) J. Chem. Phys. 102*, 5583.
9. Deligiannakis, Y., Boussac, A., and Rutherford A. W. (1995) *Biochemistry 34*, 16030.
10. Spoyalov, A. P., Huslsebosch, R. J., Shochat, S., Gast, P., and Hoff A. J. (1996) *Chem. Phys. Lett. 263*, 715.
11. Lendzian, F., Rautter, G., Käss, H., Gardiner, A., and Lubitz, W. (1996) *Ber. Bunsen-Ges. Phys. Chem. 100*, 2036.
12. Rippka, R., Deruelles, J., Waterbury, J. B., Herdmann, M., and Stanier, R. Y. (1979) *J. Gen. Microbiol. 111*, 1−61.
13. Mims, W. B. (1984) *J. Magn. Reson*. 59, 291.
14. Fauth, J. M., Schweiger, A., Braunschweiler, L., Forrer, J., and Ernst, R. (1986) *J. Magn. Reson. 66*, 64.
15. Mims, W. B. (1972) *Phys. Rev. B 6*, 3543.
16. Dikanov, S. A., and Tsvetkov, Y. D. (1992) *ESEEM Spectroscopy*, CRC Press, Boca Raton, FL.
17. Hales, B. J., and Case, E. E. (1981) *Biochim. Biophys. Acta 637*, 291.
18. Mims, W. B., and Peisach, J. (1981) in *Biological Magnetic Resonance*, Vol. 3, Chapter 5, Plenum Press, New York.
19. Lai, A., Flanagan, H. L., and Singel, D. J. (1988) *J. Chem. Phys. 89*, 7161.
20. Reijerse, E. J., and Dikanov, S. A. (1991) *J. Chem. Phys. 95*, 836.
21. Larsen, R. G., Halkides, C. J., and Singel, D. J. (1993) *J. Chem. Phys. 98*, 6705.
22. Dikanov, S. A., Tsvetkov, Y. D., Bowman, M. K., and Astashkin, A. V. (1982) *Chem. Phys. Lett. 90*, 149.
23. Käss, H., Bittersmann-Weidlich, E., Andreasson, L.-E., Boenigk, B., and Lubitz, W. (1995) *Chem. Phys. 194*, 419−432.
24. Deligiannakis, Y., and Rutherford A. W. (1997) *J. Am. Chem. Soc. 119*, 4471.
25. Flanagan, H. L., and Singel, D. J. (1987*) J. Chem. Phys. 87*, 5606.
26. Hunt, M. J., and Mackay, A. L. (1976) *J. Magn. Reson. 22*, 295.
27. Edmonds, D. T. (1977) *Phys. Rep. C 29*, 233.
28. Ashby, C. H., Paron, W. F., and Brown, T. L. (1980*) J. Am. Chem. Soc. 102*, 2290.
29. McCracken, J., Pemper, S., Benkovic, S. J., Villafranca, J. J., Miller, R. J., and Peisach, J. (1988) *J. Am. Chem. Soc. 110*, 1069.
30. Rigby, S. E. J., Evans, M. C. W., and Heathcote, P. (1996) *Biochemistry 35*, 6651.
31. Gordy, W. (1980) *Theory and Applications of Electron Spin Resonance*, pp 198−304, John Wiley & Sons, Inc., New York.
32. Lubitz, W., Abresch, E. C., Debus, R. J., Isaacson, R. A., Okamura, M. Y., and Feher, G. (1985) *Biochim. Biophys. Acta 808*, 464.
33. MacMillan, F., Lendzian, F., and Lubitz, W. (1995) *Magn. Reson. Chem. 33*, S81.
34. Nitschke, W., Feiler, U., and Rutherford, A. W. (1990) *Biochemistry 29*, 3834−3842.
35. Nitschke, W., and Rutherford, A. W. (1991) *Trends Biochem. Sci. 16*, 241−245.
36. Nitschke, W., Mattioli, T. A., and Rutherford, A. W. (1996) in *Origin and Evolution of Biological Energy Conservation* (Baltscheffsky, H., Ed.) pp 143−175, VCH Publishers.
37. Rutherford, A. W., and Nitschke, W. (1996) in *Origin and Evolution of Biological Energy Conservation* (Baltscheffsky, H., Ed.) pp 177−203, VCH Publishers.
38. Vermaas, W. F. J. (1994) *Photosynth. Res. 41*, 285−294.
39. Golbeck, J. H. (1993) *Proc. Natl. Acad. Sci. U.S.A. 90*, 1642−1646.
40. Fromme, P., Witt, H. T., Schubert, W.-D., Klukas, O., Saenger, W., and Krauss, N. (1996*) Biochim. Biophys. Acta 1275*, 76−83.
41. Webber, A. N., Hui, S., Bingham, S. E., Käss, H., Krabben, L., Kuhn, M., Jordan, R., Schlodder, E., and Lubitz, W. (1996) *Biochemistry 35*, 12857.
42. van der Est, A., Prisner, T., Bittl, R., Fromme, P., Lubitz, W., Möbius, K., and Stehlik, D. (1997) *J. Phys. Chem. B, 101*, 1437−1443.
43. Deisenhofer, J., and Michel, H. (1988) *EMBO J. 8*, 2149−2170.
44. Berry, M. C., Bratt, P. J., and Evans, M. C. W. (1997) *Biochim. Biophys. Acta 1319*, 163−176.

BI971360A